

Influence of 2-D Transceiver Array Aperture Size and Polarization on 3-D Microwave Imaging of Subsurface Objects Under Born Approximation

Kemeng Tao^{ID}, Sijia Ma^{ID}, and Feng Han^{ID}, *Senior Member, IEEE*

Abstract—This article utilizes the spectral analysis method to investigate the influence of 2-D transceiver array aperture size and polarization on 3-D qualitative microwave imaging of subsurface objects. The investigation is performed in three steps. First, in the framework of the integral equation with Born approximation (BA), we derive the analytical relationship between the 2-D spectra of the scattered electric fields and the reconstructable 3-D object spectrum, which is weighted by a vector coefficient related to transceiver polarization. The theoretically reconstructable 3-D spectrum is analyzed. Second, to obtain the 3-D spectrum for more practical microwave imaging measurement with the wave attenuation, the evanescent mode contribution, and the transceiver polarization considered, we perform the singular value decomposition (SVD) to compute the discretized integral operator right-singular function whose spectrum reflects the reconstructable 3-D spectrum. It is shown that the mutual coupling in two orthogonal horizontal directions leads to the vertical “allpass” feature and the horizontal “low-pass” feature in one vertical 2-D plane if the array aperture size in the orthogonal horizontal direction is large enough. Meanwhile, the transceiver polarization also has obvious effects on the reconstructable spectrum. Third, numerical experiments are implemented to verify the relationship between the transceiver array configuration and the reconstructable spectrum.

Index Terms—Array aperture size, full-wave inversion (FWI), microwave imaging, 3-D subsurface objects, transceiver polarization.

I. INTRODUCTION

MICROWAVE imaging (MWI) employs electromagnetic (EM) fields at frequencies ranging from hundreds of megahertz to hundreds of gigahertz to sense a given scene [1]. Due to possessing the intrinsic merit of noninvasive inspection, the core microwave diagnostic techniques have wide applications in both civil and industrial areas. They mainly include biomedical imaging [2], security check [3], near-field microscopy imaging [4], subsurface prospection [5], materials evaluation [6], circuit inspection [7], and so on.

Manuscript received 9 May 2024; accepted 15 June 2024. Date of publication 28 June 2024; date of current version 7 January 2025. This work was supported by the National Natural Science Foundation of China under Grant 62271428. (*Corresponding author: Feng Han*.)

Kemeng Tao and Sijia Ma are with the Institute of Electromagnetics and Acoustics and the Key Laboratory of Electromagnetic Wave Science and Detection Technology, Xiamen University, Xiamen 361005, China.

Feng Han is with the School of Computing and Information Technology, Great Bay University, Guangdong 523000, China, and also with the Institute of Electromagnetics and Acoustics, Xiamen University, Xiamen 361005, China (e-mail: feng.han@gbu.edu.cn; feng.han@xmu.edu.cn).

Color versions of one or more figures in this article are available at <https://doi.org/10.1109/TMTT.2024.3416330>.

Digital Object Identifier 10.1109/TMTT.2024.3416330

According to the adopted techniques and obtained image accuracy, MWI can be roughly divided into two categories, qualitative and quantitative. The commonly used qualitative approaches include tomography, sampling methods, migration, and so on. They have been widely adopted in medical diagnosis and geophysical exploration. For example, the back-propagation (BP) tomography and the diffraction tomography are frequently used to invert for organism local parameter distribution [8] and in the real-time through-the-wall imaging [9], [10]. In the linear sampling method (LSM), the target image is focused through projecting the scattered EM fields recorded at the receiver array onto a virtual radiation source point in the imaging region [11]. It has been hybridized with an artificial neural network (ANN) and EM full-wave inversion (FWI) to reconstruct multiple subsurface objects when the antenna array aperture is limited [12]. Migration methods are intensively used in the ground-penetrating radar (GPR) detection. Reverse time migration (RTM) realizes the image focusing by correlating the incident wave and the reflected wave in the timestamp of the target space position [13]. Kirchhoff migration (KM) is more efficient than RTM, but the imaging results are not as accurate as those by RTM [14]. Unfortunately, these qualitative methods can only recover the geometry information, e.g., shapes, sizes, and locations, of the subsurface objects.

The EM FWI is the most typical quantitative imaging method. It is implemented via strictly solving the wave equations and, thus, is able to simultaneously reconstruct both the geometrical and dielectric parameters. Researchers have proposed a series of FWI methods for subsurface object quantitative reconstruction, such as the Born iterative method (BIM) [15], distorted BIM (DBIM) [16], variational BIM (VBIM) [17], contrast source inversion (CSI) [18], and subspace optimization method (SOM) [19] in the past decades. Other studies further extend these methods to the hybrid ones, including subspace-based DBIM [20], cascade of VBIM and BIM solvers [21], contrast source extended Born (CSEB) method [22], and so on. In addition, there are also some novel proposed methods, such as virtual scattering experiments [23] and smart rewriting of the EM scattering equations [24], [25], to mitigate the nonlinearity in the traditional iterative FWI and, thus, to further enhance the implementation efficiency.

The aforementioned qualitative and quantitative MWI research is focused on the methods themselves as well as their applications. There is another research branch regarding

MWI used for subsurface detection, which is focused on the influence of configurations of transmitting antennas and receiving antennas on the reconstruction results. Specifically speaking, the quantitative relationships between the reconstructable spectrum bandwidth of the subsurface object and the transceiver parameters, such as the array size, the array elevation, spatial offsets between transmitters and receivers, frequency sweeping step in multifrequency measurement, and antenna radiation pattern, are analyzed by Fourier transforms and by singular value decomposition (SVD) and finally also validated in several numerical experiments of FWI. A lot of research works have been conducted under the Born approximation (BA). Thus, they are only valid for weak EM scattering and still fall into the category of qualitative MWI, although the whole framework is built on integral equations (IEs). For example, in [26], the specific relationship between the spectrum of the scattered electric field at the 1-D receiver array and the 2-D spectrum of the subsurface contrast is derived via a series of Fourier transforms starting from IEs with BA. The “lowpass” feature of the 2-D reconstructable spectrum of the subsurface object in the horizontal \hat{x} -direction and the “bandpass” feature in the vertical \hat{z} -direction caused by the limited array aperture size or the array elevation are proved and further validated by SVD analysis and numerical examples. In [27], the reconstructable spectra of subsurface objects are compared for multiview-multistatic transceivers with different offsets and different operation frequencies. In [28] and [29], the influence of the frequency hopping step on the reconstruction of subsurface objects is analyzed and validated in detail. Meanwhile, the optimized inversion strategies are suggested for multifrequency data. In [30] and [31], the influence of real antenna radiation patterns on migration imaging and FWI of subsurface objects is analyzed and validated. However, most of these works only study how the 1-D transceiver array configuration influences EM reconstruction of 2-D subsurface objects. Although, in [32] and [33], the influence of 2-D array configuration on the inversion performance of 3-D objects is analyzed under BA when the transmitters and receivers are placed on two different sides of the imaging domain and on the same side of the domain, respectively, they only dealt with the reconstruction of 3-D objects in a homogeneous air, and the effects of array single/multiple view or stations are verified. Especially, the influence of 2-D array aperture size and transceiver polarization on the 3-D reconstructable spectrum of subsurface objects are not accounted for.

In this article, we extend the previous works [26], [27], [32], [33] to 3-D EM inverse scattering scenarios for subsurface imaging and investigate how the 2-D transceiver array aperture size and polarization affect the EM microwave reconstruction of 3-D subsurface objects under BA. Compared with previous works [26], [27], this work has the following new contributions.

- 1) A different spectral relationship between scattered electric fields at the 2-D receiver array and the 3-D subsurface objects is derived based on the half-space 3-D layered medium dyadic Green’s functions (DGFs). The reconstructable 3-D spectrum is weighted by a vector coefficient that depends on the transceiver polarization.

- 2) The computed reconstructable 3-D spectrum has a strong mutual coupling in two orthogonal horizontal directions, i.e., the large array aperture size in the \hat{x} -direction can broaden the yz plane 2-D spectrum bandwidth and vice versa.
- 3) Meanwhile, due to the mutual coupling effect, the reconstructable 3-D spectrum shows the vertical “allpass” feature and the horizontal “lowpass” feature in one vertical 2-D plane if the array aperture size in the orthogonal horizontal direction is large enough. This is different from the “bandpass” feature in the vertical direction and the “lowpass” feature in the only horizontal direction for the 2-D case given in previous works [26], [27].
- 4) The mutual coupling effect as well as the spectral filtering features with the decrease of the array aperture size are analyzed by SVD of the discretized integral operator based on BA and successfully validated in numerical examples.
- 5) The effects of transceiver polarization on the reconstructable spectrum of the 3-D subsurface object are also analyzed by SVD and validated in numerical experiments. This has never been addressed in the previous works [32], [33]. Meanwhile, the aforementioned mutual coupling effect and the vertical “allpass” feature in some situations are also not dealt with in [32] and [33].

One should note that, although the previous works [28], [29] have dealt with the influence of multifrequency data on the reconstructable 2-D spectra of subsurface objects, we temporarily do not consider the effects of multifrequencies in the incident and scattered EM fields on the reconstruction in this work. The organization of this article is as follows. In Section II, the analytical relationship between the scattered electric-field spectrum at the 2-D receiver array and the spectrum of the 3-D object placed in the subsurface region is derived. Then, the influence of the 2-D transceiver array aperture size on the 3-D reconstructable spectrum of the subsurface contrast is theoretically analyzed in Section III and is numerically analyzed by SVD in Section IV when the wave attenuation in the subsurface region and the evanescent mode are considered. Meanwhile, the influence of the transceiver polarization on the reconstructable spectrum is also analyzed by SVD. In Section V, both the theoretical and numerical analysis results are validated in numerical experiments. Finally, in Section VI, the conclusion and the possible future work are presented.

II. THREE-DIMENSIONAL EM LINEAR INVERSE SCATTERING IN SUBSURFACE DETECTION

As shown in Fig. 1, the background 3-D space is separated by a planar interface located at $z = 0$. The transmitter and receiver arrays are located in the $z < 0$ region, which has the dielectric parameters ϵ_0 and μ_0 . The 3-D scatterer is located in the $z > 0$ region, which has the complex relative permittivity $\epsilon_b = \epsilon_b + (\sigma_b/j\omega\epsilon_0)$ and the permeability μ_0 . The inhomogeneous scatterer with the spatially varying relative permittivity $\epsilon_s(\mathbf{r})$ and conductivity $\sigma_s(\mathbf{r})$ is placed inside the cuboid inversion domain D with the dimensions

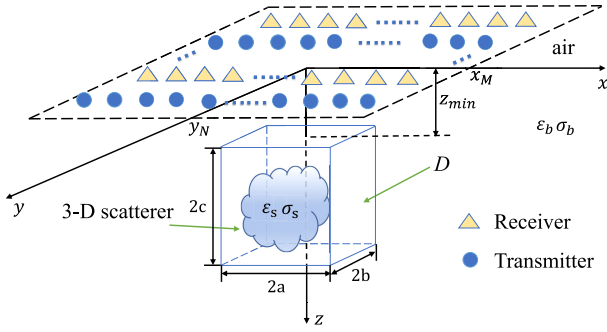


Fig. 1. Configuration of the 3-D EM inverse scattering from inhomogeneous objects buried in the subsurface domain D with the dimensions of $2a \times 2b \times 2c$.

of $2a \times 2b \times 2c$. The upper surface of the domain D is located at $z = z_{\min}$. Both the transmitter and receiver arrays have the horizontal sizes of $2x_M \times 2y_N$. The transmitter array is located at the $z = z_s$ plane, while the receiver array is located at the $z = z_r$ plane. The scattered electric field at a receiver point \mathbf{r}_r is evaluated by

$$\mathbf{E}^{\text{sct}}(\mathbf{r}_r) = j\omega\epsilon_b\epsilon_0 \int_D \bar{\bar{\mathbf{G}}}(\mathbf{r}_r, \mathbf{r}) \cdot \mathbf{E}^{\text{tot}}(\mathbf{r}) \chi(\mathbf{r}) d\mathbf{r} \quad (1)$$

where

$$\chi(\mathbf{r}) = \frac{\epsilon_s(\mathbf{r}) - \epsilon_b}{\epsilon_b} \quad (2)$$

is the contrast of the scatterer, $\bar{\bar{\mathbf{G}}}$ is the layered medium DGF linking a field point \mathbf{r} inside the inversion domain D and the receiver point \mathbf{r}_r , and \mathbf{E}^{tot} is the total electric field inside D when the inhomogeneous scatterer is present. Since we focus on qualitative MWI and only consider the weak scattering scenarios in this work, (1) is linearized by BA

$$\mathbf{E}^{\text{sct}}(\mathbf{r}_r) = j\omega\epsilon_b\epsilon_0 \int_D \bar{\bar{\mathbf{G}}}(\mathbf{r}_r, \mathbf{r}) \cdot \mathbf{E}^{\text{inc}}(\mathbf{r}) \chi(\mathbf{r}) d\mathbf{r} \quad (3)$$

where \mathbf{E}^{inc} is the incident electric field inside the inversion domain D when the scatterer is absent, and it is evaluated by

$$\mathbf{E}^{\text{inc}}(\mathbf{r}) = \bar{\bar{\mathbf{G}}}(\mathbf{r}, \mathbf{r}_s) \cdot \mathbf{J}(\mathbf{r}_s) \quad (4)$$

in which $\bar{\bar{\mathbf{G}}}$ is the layered medium DGF linking the source point \mathbf{r}_s and the field point \mathbf{r} inside D and \mathbf{J} is the current density of the infinitesimal dipole transmitter at \mathbf{r}_s . According to the transmission-line analogy method given in [34], the layered medium DGF $\bar{\bar{\mathbf{G}}}$ can be computed by the 2-D inverse Fourier transforms

$$\bar{\bar{\mathbf{G}}}(\mathbf{r}_r, \mathbf{r}) = \frac{1}{4\pi^2} \iint_{-\infty}^{+\infty} \tilde{\mathbf{G}}(\mathbf{k}_\rho, z_r, z) e^{-j\mathbf{k}_\rho \cdot \rho} d\mathbf{k}_\rho \quad (5a)$$

$$\bar{\bar{\mathbf{G}}}(\mathbf{r}, \mathbf{r}_s) = \frac{1}{4\pi^2} \iint_{-\infty}^{+\infty} \tilde{\mathbf{G}}(\mathbf{k}'_\rho, z, z_s) e^{-j\mathbf{k}'_\rho \cdot \rho'} d\mathbf{k}'_\rho \quad (5b)$$

where $\tilde{\mathbf{G}}$ is the spectral-domain DGF in a layered medium whose specific expression is given in Appendix A and $\rho = \hat{x}(x_r - x) + \hat{y}(y_r - y)$ is the horizontal vector pointing from the field point \mathbf{r} to the receiver point \mathbf{r}_r , $\rho' = \hat{x}(x - x_s) + \hat{y}(y - y_s)$ is the horizontal vector pointing from the source point \mathbf{r}_s to the field point \mathbf{r} , and $\mathbf{k}_\rho = \hat{x}k_x + \hat{y}k_y$ and $\mathbf{k}'_\rho = \hat{x}k'_x + \hat{y}k'_y$ are wavenumber vectors. By substituting (5b) into (4), substituting (5a) into (3), and substituting (4) into (3),

we can obtain

$$\begin{aligned} \mathbf{E}^{\text{sct}}(\mathbf{r}_r) &= \frac{j\omega\epsilon_b\epsilon_0}{16\pi^4} \int_D \iint_{-\infty}^{+\infty} \iint_{-\infty}^{+\infty} \tilde{\mathbf{G}}(\mathbf{k}_\rho, z_r, z) \tilde{\mathbf{G}}(\mathbf{k}'_\rho, z, z_s) \\ &\quad e^{-j\mathbf{k}'_\rho \cdot \rho'} e^{-j\mathbf{k}_\rho \cdot \rho} d\mathbf{k}'_\rho d\mathbf{k}_\rho \cdot \mathbf{J}(\mathbf{r}_s) \chi(\mathbf{r}) d\mathbf{r} \\ &= \frac{j\omega\epsilon_b\epsilon_0}{16\pi^4} \int_D \iint_{-\infty}^{+\infty} \iint_{-\infty}^{+\infty} \tilde{\mathbf{G}}(\mathbf{k}_\rho, z_r, z) \tilde{\mathbf{G}}(\mathbf{k}'_\rho, z, z_s) \cdot \mathbf{J}(\mathbf{r}_s) \\ &\quad e^{-j(k'_x - k_x)x} \cdot e^{-j(k'_y - k_y)y} \cdot e^{jk'_x x_s} \cdot e^{jk'_y y_s} \cdot e^{-jk_x x_r} \cdot e^{-jk_y y_r} dk'_x dk'_y dk_x dk_y \\ &\quad dx dy dz \end{aligned} \quad (6)$$

where the detailed expression of $\tilde{\mathbf{G}}(\mathbf{k}_\rho, z_r, z) \tilde{\mathbf{G}}(\mathbf{k}'_\rho, z, z_s) \cdot \mathbf{J}(\mathbf{r}_s)$ can be found in Appendix B. Then, we make following definitions:

$$\begin{cases} \eta = k'_x - k_x \\ \tau = k'_y - k_y \\ \zeta = k'_{z2} + k_{z2} \end{cases} \quad (7a)$$

$$\widehat{\chi}(\eta, \tau, \zeta) = \int_D \chi(x, y, z) e^{-j\eta x} e^{-j\tau y} e^{-j\zeta z} dx dy dz. \quad (7b)$$

Thus, (6) can be rewritten as follows:

$$\begin{aligned} \mathbf{E}^{\text{sct}}(\mathbf{r}_r) &= \frac{j\omega\epsilon_b\epsilon_0}{16\pi^4} \iint_{-\infty}^{+\infty} \iint_{-\infty}^{+\infty} \mathbf{f} \cdot \widehat{\chi} \\ &\quad \cdot e^{jk'_x x_s} \cdot e^{jk'_y y_s} \cdot e^{-jk_x x_r} \cdot e^{-jk_y y_r} dk'_x dk'_y dk_x dk_y \end{aligned} \quad (8)$$

where \mathbf{f} is determined by the transceiver polarization. Its expression can be found in Appendix B. Finally, we assume that the transmitter array and the receiver array are located at the same altitude, i.e., $z_s = z_r$, and define the spectrum of the scattered electric field at the receiver array as follows:

$$\begin{aligned} \widetilde{\mathbf{E}}^{\text{sct}}(k_x, k'_x, k_y, k'_y) &= \iint_{-\infty}^{+\infty} \iint_{-\infty}^{+\infty} \mathbf{E}^{\text{sct}}(x_s, x_r, y_s, y_r) \\ &\quad e^{-jk'_x x_s + jk_x x_r} \cdot e^{-jk'_y y_s + jk_y y_r} dx_s dx_r dy_s dy_r. \end{aligned} \quad (9)$$

Thus, (8) can be expressed in a compact form

$$\widetilde{\mathbf{E}}^{\text{sct}} = j\omega\epsilon_b\epsilon_0 \cdot \mathbf{f}(k_x, k'_x, k_y, k'_y) \cdot \widehat{\chi}. \quad (10)$$

Obviously, \mathbf{f} weights the spectrum of the contrast distribution inside the inversion domain D , which can be retrieved from the spectrum of the scattered electric field at the receiver array.

III. INFLUENCE OF THE 2-D TRANSCEIVER ARRAY APERTURE SIZE ON 3-D SUBSURFACE FWI WITH BA: THEORETICAL ANALYSIS

In this section, we give a theoretical analysis of how the 2-D transceiver array aperture size influences the 3-D inversion of subsurface objects with BA. Specifically speaking, we evaluate the quantitative relationship between the transceiver array aperture size and the spectrum bandwidth of the reconstructable 3-D contrast χ . Meanwhile, we also analyze and explain the mutual coupling of the reconstructable 3-D spectrum in two orthogonal horizontal directions, which has never been discussed in previous works. For convenience to perform theoretical analysis, we suppose both the subsurface background medium and the 3-D scatterer are lossless,

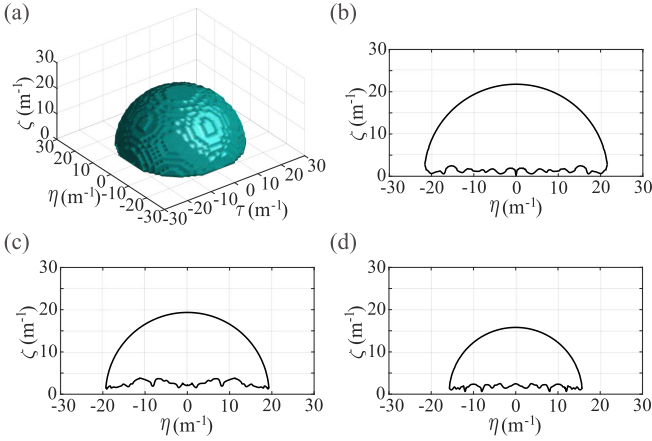


Fig. 2. Theoretically reconstructable spectrum of the subsurface 3-D scatterer contrast when the transceiver arrays have infinitely large aperture sizes. (a) Three-dimensional spectrum. (b) Two-dimensional $\eta\zeta$ slice of the spectrum at $\tau = 0 m^{-1}$. (c) Two-dimensional $\eta\zeta$ slice of the spectrum at $\tau = 10 m^{-1}$. (d) Two-dimensional $\eta\zeta$ slice of the spectrum at $\tau = 15 m^{-1}$.

i.e., $\sigma_b = 0$ and $\sigma_s(x, y, z) = 0$. The operation frequency is 300 MHz. Other parameters related to the inversion domain D are $\varepsilon_b = 3.0$, $a = b = c = 0.6$ m, and $z_{\min} = 0.4$ m. Meanwhile, it is assumed that the inversion domain D is far enough from the horizontal interface, and thus, the effect of the evanescent wave on the computation of the theoretically reconstructable spectrum of the 3-D scatterer contrast is neglected. Note that the “theoretically” here means the computed spectra are not influenced by the transceiver polarization, noise contamination, subsurface signal attenuation, and so on. They are only determined by the valid wavenumber ranges avoiding the evanescent mode.

Let us first discuss the extreme case in which the 2-D transceiver array aperture size shown in Fig. 1 is infinitely large, i.e., $x_M = +\infty$ and $y_N = +\infty$. In this situation, the spectra of the electric fields at the receiver array evaluated according to (9) correspond to the scattered fields sampled at a 2-D infinitely large plane. In other words, all the spatial-domain scattered electric-field information generated by the scatterers buried inside D is incorporated into the spectra of the scattered fields. Therefore, based on (10), we can claim that the 2-D transceiver array aperture size has no harm to the reconstructed 3-D contrast. The reconstructable $\hat{\chi}$ distribution is completely determined by the valid wavenumber values of the incident and scattered EM waves given in (7a). As long as $k'_\rho = (k_x^2 + k_y^2)^{1/2}$ is real and less than $k_b = \omega(\varepsilon_b \varepsilon_0 \mu_0)^{1/2}$ and $k_\rho = (k_x^2 + k_y^2)^{1/2}$ is real and also less than k_b , both the incident and scattered EM waves are not evanescent. As a result, both of them can effectively propagate between the transceiver array and the inversion domain D , and thus, the ranges of k'_x , k'_y , k_x , and k_y satisfying the aforementioned conditions determine the ranges of η , τ , and ζ in (7a), which finally determine the reconstructable spectrum of the 3-D scatterer contrast. It is shown in Fig. 2(a), and its 2-D $\eta\zeta$ slices for different τ values are shown in Fig. 2(b)–(d). The roughness of the curve near the $\zeta = 0$ plane is caused by a lot of numerical tries of different values of k'_x , k_x , k'_y , and k_y subject to the definitions given in (7a) when

k'_z and $k_z \rightarrow 0$. Note that the 2-D $\tau\zeta$ slice is not shown here, because it is exactly the same as the $\eta\zeta$ one due to symmetry. We can see that the slices of the 3-D reconstructable spectrum are similar to the largest area surrounded by the solid black line shown in [26, Fig. 2]. The spectrum in the $\hat{\eta}$ -, $\hat{\tau}$ -, or $\hat{\zeta}$ -direction has a limited bandwidth. The spectral contents located outside the reconstructable band represent the nonretrievable χ information, which actually corresponds to the evanescent waves that cannot reach the transceiver array and are generated when k'_ρ is imaginary, k_ρ is imaginary, $(k_x^2 + k_y^2)^{1/2} > k_b$, or $(k_x^2 + k_y^2)^{1/2} > k_b$. The most obvious difference between the 3-D reconstructable spectrum and the 2-D one shown in [26, Fig. 2] is missing the “holes.” In other words, the 2-D spectrum shows a “bandpass” feature in the vertical \hat{z} -direction, while the 3-D spectrum shows an “allpass” feature. The root reason for such a difference is the mutual coupling of the reconstructable spectrum in two orthogonal horizontal directions. From a mathematical point of view, the loss of low-frequency contents in the vertical \hat{z} -direction of the reconstructable 2-D spectrum shown in [26, Fig. 2] is because k'_{z2} and k_{z2} in (7a) cannot simultaneously take small values. In a 2-D problem, the k'_{z2} values are uniquely constrained by k'_x via $(k'_{z2}^2 + k_x'^2)^{1/2} = k_b$, while k_{z2} values are also uniquely constrained by k_x via $(k_{z2}^2 + k_x^2)^{1/2} = k_b$. Obviously, the low-frequency contents in the vertical \hat{z} -direction require k_x and k'_x simultaneously approach k_b or $-k_b$, which, however, leads to the almost same or opposite values of k_x and k'_x . These two situations are corresponding to the three points $(\eta, \zeta) = (-2k_b, 0) m^{-1}$, $(\eta, \zeta) = (0, 0) m^{-1}$, and $(\eta, \zeta) = (2k_b, 0) m^{-1}$ in [26, Fig. 2], since $\eta = k'_x - k_x$. In other sampling points, η falls in the range of $0 < |\eta| < 2k_b$, which requires k_x and k'_x take different values and are not equal to $-k_b$ or k_b . As a result, k_x and k'_x cannot simultaneously approach k_b or $-k_b$, and thus, the low-frequency contents in the vertical \hat{z} -direction are lost. In physics, this is not difficult to understand. The low-frequency contents in the 2-D reconstructable spectrum shown in [26, Fig. 2] indicate the severe suppression of the vertical spatial resolution, which requires both the incident EM wave and the scattered EM wave almost lying in the horizontal \hat{x} -direction, i.e., $k'_x \rightarrow \pm k_b$ and $k_x \rightarrow \pm k_b$. Consequently, for the vertical low-frequency contents, the horizontal resolution of the reconstruction only can choose two distinct values, the maximum value when k_x and k'_x are almost opposite and the minimum value when k_x and k'_x simultaneously approach k_b or $-k_b$. However, in the 3-D case, the situation is completely different. Although we also force the incident EM wave and the scattered EM wave almost lying in the horizontal xy plane to suppress vertical resolution in the reconstruction, the constraints of the wavenumbers become $(k_x'^2 + k_y'^2)^{1/2} \rightarrow k_b$ and $(k_x^2 + k_y^2)^{1/2} \rightarrow k_b$. As a result, both the incident and scattered wavenumbers can be selected in a series of combinations instead of only being approaching $\pm k_b$. The spatial frequency $\eta = k'_x - k_x$ and $\tau = k'_y - k_y$ reflecting the horizontal resolution will also change between 0 and $\pm 2k_b$ instead of only taking the distinct value of 0 or $\pm 2k_b$. From a physical point of view, the horizontal incident EM wave can impinge on the subsurface 3-D scatterer from a series of different azimuthal angles, and the scattered EM waves can also escape away from the

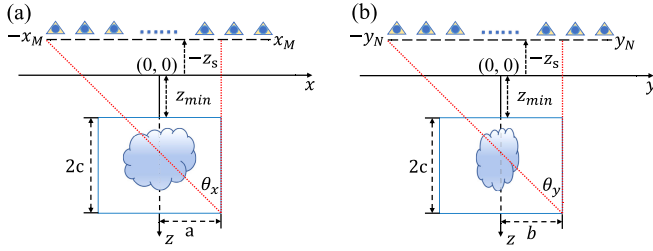


Fig. 3. Definition of the array angle used to denote the array aperture size. (a) θ_x in the xz plane. (b) θ_y in the yz plane.

scatterer at different azimuthal angles, which naturally widens the horizontal spatial spectrum bandwidth of the reconstruction for the vertical low-frequency contents. Since the 2-D infinitely large aperture size does not exist in reality, we will not discuss it anymore in this work.

So, let us now focus on how the limited 2-D aperture size of the transceiver array affects the subsurface 3-D reconstruction results. In this situation, from a physical point of view, partial information of the scattered electric fields generated by the scatterers buried inside D is lost, since the 2-D transceiver array does not extend infinitely far. Mathematically, the integration in (9) is only performed within a truncated domain. $\tilde{\mathbf{E}}^{\text{sct}}$ in (10) used to infer the 3-D spectrum of the subsurface contrast χ fails to accurately represent true scattered electric fields generated by the scatterers. Consequently, the reconstructed subsurface 3-D scatterers will have distorted shapes. In the spectral domain, the effective bandwidth will become narrower. In order to quantitatively explore this, we take the same approximation suggested in [26, Sec. III] and reflect the aperture size change in the valid wavenumber value. It is assumed that the dominant energy of the scattered EM wave is propagating from a fictitious equivalent source point inside the domain D to a receiver like a plane wave. Similarly, the major energy of the incident EM wave from a certain transmitter to the inversion domain also behaves like a plane wave. Reducing the 2-D array size, i.e., decreasing x_M and y_N , is equivalent to decreasing the array angles θ_x and θ_y defined in Fig. 3. Therefore, obeying the plane wave assumptions mentioned above, the valid wavenumbers automatically satisfy

$$|k_x|, |k'_x| < k_b \sin \theta_x = \frac{k_b |x_M + a|}{\sqrt{(x_M + a)^2 + (z_{min} + 2c + z_s)^2}} \quad (11a)$$

$$|k_y|, |k'_y| < k_b \sin \theta_y = \frac{k_b |y_N + b|}{\sqrt{(y_N + b)^2 + (z_{min} + 2c + z_s)^2}} \quad (11b)$$

where it has been supposed $z_s = z_r$. We now let k_x , k'_x , k_y , and k'_y be subject to the inequality in (11) in accord with the transceiver array aperture size limitation and simultaneously let $(k_x^2 + k_y^2)^{1/2} < k_b$ and $(k_x^2 + k_y^2)^{1/2} < k_b$ to guarantee both the incident and scattered waves can normally propagate and finally obtain the 3-D reconstructable spectrum of the subsurface scatterer contrast. In order to vividly show how the reconstructable 3-D spectrum varies with the aperture size when $z_s = z_r = 0.0$ m, we let x_M or y_N take five typical values

0.0, 0.25, 1.0, 2.25, and 7.5 m. The corresponding five values of θ_x or θ_y are 0° , 28° , 45° , 60° , and 79° , respectively. Fig. 4 shows the theoretically reconstructable 3-D spectra of the scatterer contrasts for different combinations of θ_x and θ_y values. Their 2-D $\eta\zeta$ slices at $\tau = 0$ are shown in Fig. 5(a)–(e), while the 2-D $\tau\zeta$ slices at $\eta = 0$ are shown in Fig. 5(f)–(j). Three observations are made. First, the reconstructable 3-D bandwidth becomes narrower compared with that for the infinitely large aperture size shown in Fig. 2. Reducing the 2-D array aperture size directly filters out the high-frequency contents of the 3-D reconstructable spectrum in the horizontal xy plane. In mathematics, reducing the transceiver array aperture size is equivalent to decreasing the maximum valid values of k'_x , k_x , k'_y , and k_y according to (11), which results in the reduction of the valid ranges of η and τ in (7a). In physics, reducing the transceiver array aperture size lowers the horizontal resolution of the reconstruction, which is equivalent to filtering out the high-frequency contents of the spectrum. Second, by contrast, in the vertical \hat{z} -direction, reducing the array aperture size filters out the low-frequency contents in the 3-D reconstructable spectrum and, thus, leads to the “bandpass” phenomenon. When the maximum values of k'_x , k_x , k'_y , and k_y decrease, the minimum values of k'_{z2} and k_{z2} increase, which leads to the increase of the minimum value of ζ according to (7a). In physics, the EM wave energy is more constrained in the vertical \hat{z} -direction, and thus, the high-frequency contents of the reconstructable spectrum in the vertical direction are magnified, but the low-frequency contents are suppressed. Third, the sizes of the “holes” shown in Fig. 5(f)–(j) indicating the loss extent of the low-frequency contents in the vertical \hat{z} -direction not only increase with the transceiver array aperture size decrease in the \hat{y} -direction but also depend on array aperture size in the \hat{x} -direction. In the extreme case when θ_x becomes 79° , the “holes” for all θ_y values disappear, as shown in Fig. 5(j). In this situation, the “bandpass” feature of the reconstructable spectrum in the vertical direction becomes an “allpass” feature. In other words, the mutual coupling in two orthogonal horizontal directions broadens the 3-D reconstructable spectrum bandwidth. In mathematics, the mutual coupling is because θ_x also affects the range of τ when ζ approaches zero. The value of θ_x directly restricts k'_x and k_x varying between $-k_b \sin \theta_x$ and $k_b \sin \theta_x$. Therefore, for small ζ values in the 3-D reconstructable spectrum representing the low-frequency contents in the vertical \hat{z} -direction, $|k'_y|$ and $|k_y|$ are approximately restricted between $k_b \cos \theta_x$ and $k_b \sin \theta_y$, which further restricts the range of τ in (7a). Therefore, as shown in Fig. 5(f)–(j), for $\zeta \rightarrow 0$, the τ values are restricted by $-2k_b \sin \theta_y < \tau < -2k_b \cos \theta_x$ and $2k_b \cos \theta_x < \tau < 2k_b \sin \theta_y$. For a large θ_x value, the restriction almost becomes $-2k_b \sin \theta_y < \tau < 2k_b \sin \theta_y$, and thus, the vertical “bandpass” feature becomes the “allpass” feature. In physics, both the incident and scattered waves must almost be restricted in the horizontal plane to achieve the low-frequency reconstruction in the vertical \hat{z} -direction. When the transceiver array aperture size is large in the \hat{x} -direction, the horizontal EM wave can impinge on and escape away from the scatterer at different angles, and thus, the horizontal spatial spectrum bandwidth for the vertical low-frequency contents is naturally broadened.

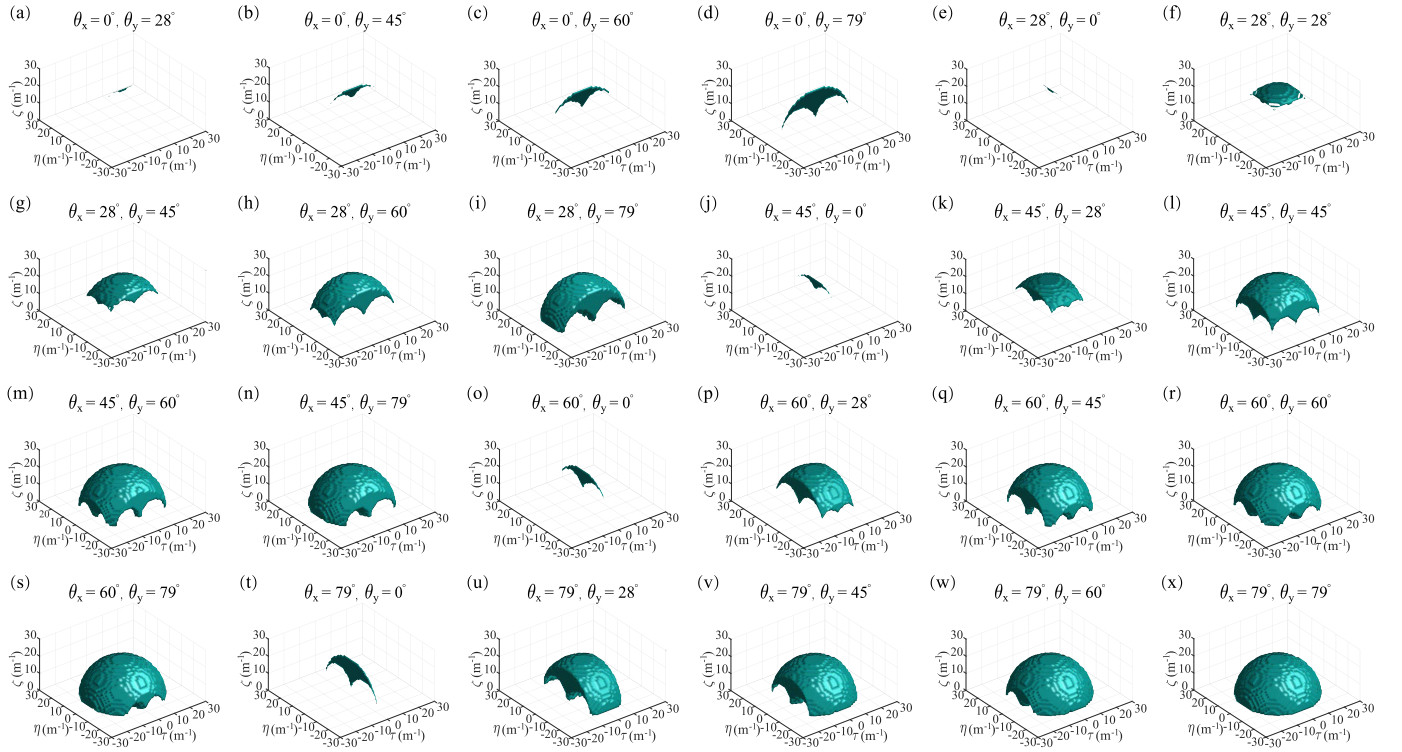


Fig. 4. Typical theoretically reconstructable 3-D spectra of the scatterer contrasts when the transceiver arrays have different aperture sizes denoted by different angles. The corresponding values are annotated in the titles of subfigures.

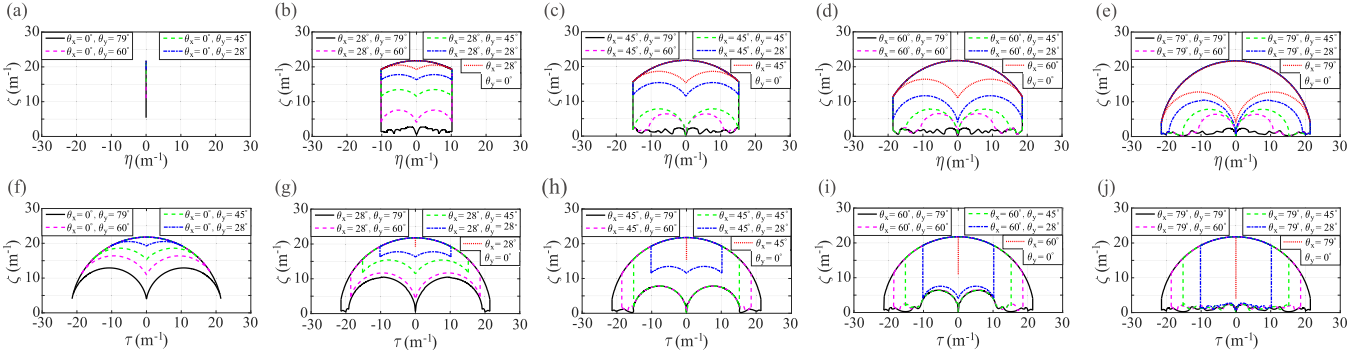


Fig. 5. Two-dimensional slices of the 3-D spectra shown in Fig. 4. The first row shows the $\eta\zeta$ slices at $\tau = 0$. The second row shows the $\tau\zeta$ slices at $\eta = 0$. Each theoretical 2-D spectrum is enclosed within a closed curve.

IV. INFLUENCE OF THE 2-D TRANSCEIVER ARRAY APERTURE SIZE AND POLARIZATION ON 3-D SUBSURFACE FWI WITH BA: SVD ANALYSIS

In this section, we consider more practical EM inverse scattering scenarios for subsurface detection. The wave attenuation in the subsurface region, the contribution from the evanescent mode, and the transceiver polarization are all incorporated in the analysis of the 3-D reconstructable spectrum of the subsurface object. Consequently, the relationship between the spectrum of the scattered EM field in the 2-D transceiver array plane and the reconstructable spectrum of the 3-D subsurface scatterer described in (10) is no longer precise. Therefore, we adopt the SVD method proposed in [26, Sec. IV] to search for the solution χ distribution of the EM inverse scattering problem described in (6).

To this end, we define the linear integral operator \mathcal{I} , which maps the χ distribution inside the 3-D subsurface inversion

domain to the scattered field data in the 2-D transceiver array

$$\mathcal{I} : \chi \in \mathcal{M} \rightarrow \mathbf{E}^{\text{sct}} \in \mathcal{D} \quad (12)$$

where \mathcal{M} is the model space within which the best solution of χ is searched for and \mathcal{D} is the 3-D data space in which the 3-D scattered electric-field data distribute. Meanwhile, it is assumed that both \mathcal{M} and \mathcal{D} are Hilbert spaces, and the L^2 inner products denoted by $\langle \cdot, \cdot \rangle_{\mathcal{M}}$ and $\langle \cdot, \cdot \rangle_{\mathcal{D}}$ can be, respectively, defined for them. Since \mathcal{I} acts on \mathcal{M} and \mathcal{D} continuously, it can be treated as a compact operator [35], and thus, SVD is allowed to apply to \mathcal{I} . Therefore, we define its singular system $\{\Sigma_n, \mathbf{U}_n, \mathbf{V}_n\}_{n=1}^{\infty}$, where Σ_n is the n th singular value, \mathbf{U}_n is the n th left-singular function, and \mathbf{V}_n is the n th right-singular function. The reconstructed χ in (6) can be written as follows [35]:

$$\chi = \sum_{n=1}^{\infty} \frac{1}{\Sigma_n} \langle \mathbf{E}^{\text{sct}}, \mathbf{U}_n \rangle_D \mathbf{V}_n \quad (13)$$

where χ is a column vector containing all the contrast values in the whole 3-D inversion domain and Σ_n decreases with the increase of n . Small Σ_n values lead to the unstable solution of the contrast, and the stable one is determined by large singular values. Therefore, we approximate the contrast solution using the truncated SVD expansion [36]

$$\chi \approx \sum_{n=1}^N \frac{1}{\Sigma_n} < \mathbf{E}^{\text{sct}}, \mathbf{U}_n >_D \mathbf{V}_n \quad (14)$$

where N is the threshold for singular values and determined according to a hypothetical signal noise ratio (SNR). Such a truncation only takes the first N singular values, restricts the χ solution to a subspace of the whole model space \mathcal{M} spanned by the first N right-singular functions, and effectively suppresses the amplification of the scattered field data error to guarantee the solution stability.

Because the operator \mathcal{I} is continuous, the SVD on it can only be performed numerically. The basic idea is to discretize the whole system. First, the 3-D inversion domain D is discretized into $M \times P \times Q$ cubic voxels. The contrast function χ is expanded by 1-D piecewise constant functions in three directions

$$\chi(x, y, z) = \sum_{m,p,q} \chi_{mpq} \cdot \Pi(x - x_m; \Delta x) \cdot \Pi(y - y_p; \Delta y) \cdot \Pi(z - z_q; \Delta z) \quad (15)$$

where $\Delta x = (2a/M)$, $\Delta y = (2b/P)$, and $\Delta z = (2c/Q)$ are the supports of the 1-D piecewise constant function in the \hat{x} -, \hat{y} -, and \hat{z} -directions, respectively, and χ_{mpq} is the expansion coefficient. Then, we substitute (15) into (6), separately execute $\int_D \{\cdot\} dx$, $\int_D \{\cdot\} dy$, and $\int_D \{\cdot\} dz$ with respect to χ based on the expression of $\tilde{\mathbf{G}}$ given in Appendix A, and obtain

$$\hat{\phi}_m = 2 \frac{\sin[(k'_x - k_x)(\frac{\Delta x}{2})]}{k'_x - k_x} e^{-j(k'_x - k_x)x_m} \quad (16a)$$

$$\hat{v}_p = 2 \frac{\sin[(k'_y - k_y)(\frac{\Delta y}{2})]}{k'_y - k_y} e^{-j(k'_y - k_y)y_p} \quad (16b)$$

$$\hat{\psi}_q = 2 \frac{\sin[(k'_{z2} + k_{z2})(\frac{\Delta z}{2})]}{k'_{z2} + k_{z2}} e^{-j(k'_{z2} + k_{z2})z_q} \quad (16c)$$

where x_m , y_p , and z_q are the central coordinates of the 1-D constant functions. Finally, by substituting (16) into (6), we obtain the approximation

$$\begin{aligned} \mathbf{E}^{\text{sct}}(\mathbf{r}_s, \mathbf{r}_s) \approx & \frac{j\omega\epsilon_b\epsilon_0}{16\pi^4} \sum_{m,p,q} \chi_{mpq} \iiint_{-\infty}^{+\infty} \mathbf{f}(k'_x, k_x, k'_y, k_y) \\ & \cdot \hat{\phi}_m(k'_x, k_x) \cdot \hat{v}_p(k'_y, k_y) \cdot \hat{\psi}_q(k'_x, k_x, k'_y, k_y) \\ & \cdot e^{-j(k_x x_s - k'_x x_s)} \cdot e^{-j(k_y y_s - k'_y y_s)} dk'_x dk_x dk'_y dk_y \end{aligned} \quad (17)$$

in which the polarization of the excitation source and which component of the scattered electric field is used in the inversion are completely reflected in \mathbf{f} . We then sample the scattered electric fields in a series of discrete points (x_s, y_s) at the $z = z_s$ horizontal plane when the excitation dipole sources also are

located in a series of discrete points (x_s, y_s) at the $z = z_s$ plane. As a result, (17) can be compactly rewritten as follows:

$$\mathbf{E}^{\text{sct}} = \mathbf{A}\chi \quad (18)$$

where \mathbf{A} is actually the discrete matrix form of the integral operator \mathcal{I} defined in (12). We now suppose there are N_{tx} and N_{ty} transmitters in the \hat{x} - and \hat{y} -directions, respectively, and N_{rx} and N_{ry} receivers in the \hat{x} - and \hat{y} -directions, respectively. Meanwhile, it is assumed $N_{rx} = N_{tx}$ and $N_{ry} = N_{ty}$ in this work, because we let the transmitter array and the receiver array completely overlap. So, the dimensions of \mathbf{A} depend on the receiver polarization, i.e., which electric component is used in the FWI. For example, when we neglect the transceiver polarization, i.e., let \mathbf{f} in (10) be one, \mathbf{A} has the dimensions of $N_{tx}N_{ty}N_{rx}N_{ry} \times MPQ$. By contrast, if we use all three components E_x^{sct} , E_y^{sct} , and E_z^{sct} in the FWI, \mathbf{A} has the dimensions of $3N_{tx}N_{ty}N_{rx}N_{ry} \times MPQ$. These issues will be discussed later in detail. In addition, one should note that the evaluation of all elements in \mathbf{A} has an unaffordable computational cost due to the fourfold integral. Fortunately, it can be lowered by two nested fast Fourier transforms, and the details will not be discussed here.

Now, let us check how the transceiver array aperture size affects the 3-D reconstructable spectrum when the transceiver polarization is neglected, but the subsurface wave attenuation and evanescent mode contribution are considered. In this situation, the dimensions of \mathbf{A} are $N_{tx}N_{ty}N_{rx}N_{ry} \times MPQ$, and \mathbf{f} is set as one. We pick five representative transceiver array aperture sizes from those shown in Figs. 4 and 5 and apply SVD to the corresponding \mathbf{A} matrices to compute the singular value distributions. These five aperture sizes are $\{\theta_x = 0^\circ, \theta_y = 79^\circ\}$, $\{\theta_x = 28^\circ, \theta_y = 79^\circ\}$, $\{\theta_x = 45^\circ, \theta_y = 79^\circ\}$, $\{\theta_x = 45^\circ, \theta_y = 45^\circ\}$, and $\{\theta_x = 45^\circ, \theta_y = 0^\circ\}$, respectively. The widths of the array apertures are $\{x_M = 0.0 \text{ m}, y_N = 7.5 \text{ m}\}$, $\{x_M = 0.25 \text{ m}, y_N = 7.5 \text{ m}\}$, $\{x_M = 1.0 \text{ m}, y_N = 7.5 \text{ m}\}$, $\{x_M = 1.0 \text{ m}, y_N = 1.0 \text{ m}\}$, and $\{x_M = 1.0 \text{ m}, y_N = 0.0 \text{ m}\}$, respectively. In addition, to account for the subsurface wave attenuation, we set the conductivity of the subsurface background to be $\sigma_b = 0.001 \text{ S/m}$. Other model parameters and the operation frequency are the same as those mentioned in Section III. The obtained normalized singular value variations for five cases are shown in Fig. 6(a). Three observations are made here. First, it seems that the variation of the singular values for a certain transceiver array aperture size is even smoother than that shown in [26, Fig. 3]. Compared with the 2-D case in which only the interface reflection and evanescent wave affect the scattered electric fields at the receiver array, the additional dimensionality in the current problem also increases the scattered field complexity, and thus, its degrees of freedom become larger. Second, the larger is the 2-D array aperture size, the more singular values are observed for a certain SNR threshold. This is as we expect. A larger aperture size implies better reconstruction resolution and broader reconstructable spectrum bandwidth, which naturally requires more singular values to recover the contrast distribution inside the inversion domain D . This will be further validated in the following spectral analysis of right-singular functions. Third, the singular value numbers for a

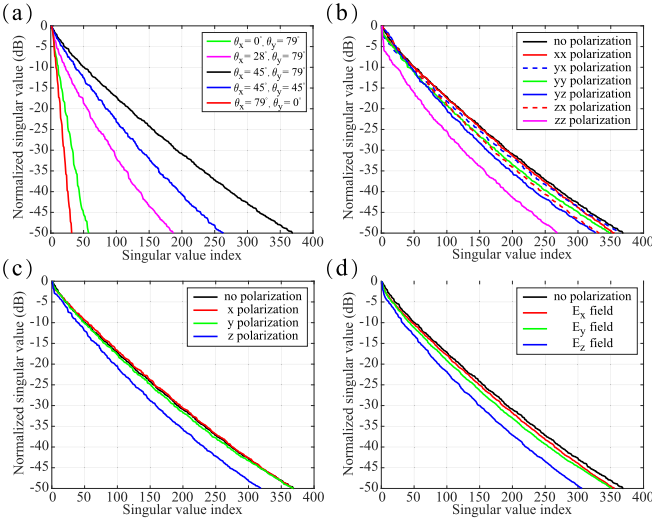


Fig. 6. Normalized singular values of the discrete integral operator \mathcal{I} for different transceiver array aperture sizes and polarizations. (a) Five representative aperture sizes with the transceiver polarization neglected. (b) Single aperture size of $\{\theta_x = 45^\circ, \theta_y = 79^\circ\}$ with different transceiver polarizations. The “yx polarization” in the legend means the unit electric dipole source points at the \hat{y} -direction, and the E_x component is used in inversion. (c) Single aperture size of $\{\theta_x = 45^\circ, \theta_y = 79^\circ\}$ with a single polarization for the transmitter but all electric-field components used in FWI. (d) Single aperture size of $\{\theta_x = 45^\circ, \theta_y = 79^\circ\}$ with the mixed $[1 \ 1 \ 1]^T$ polarization for the transmitter but a single polarization for the receiver. The $[1 \ 1 \ 1]^T$ means the unit electric dipole source has the same intensity in the \hat{x} -, \hat{y} -, and \hat{z} -directions.

certain SNR threshold do not monotonically change with the aperture size in the \hat{x} - or \hat{y} -direction. For example, the array aperture size with $\theta_x = 45^\circ$ and $\theta_y = 45^\circ$ has more singular values than that with $\theta_x = 28^\circ$ and $\theta_y = 79^\circ$. In other words, in a 3-D subsurface MWI problem, the 3-D reconstructable spectrum bandwidth is not dominated by the 2-D array size in a single direction.

Then, let us focus on the influence of transceiver polarization on the singular value distribution of the matrix \mathbf{A} . Note that the transceiver polarization is completely manifested in the coefficient \mathbf{f} whose expression is given in Appendix B. We take the transceiver aperture size $\{\theta_x = 45^\circ, \theta_y = 79^\circ\}$ as an example and consider three transceiver polarization cases, a single polarization for both the transmitter and receiver, a single polarization for the transmitter but all electric-field components used in FWI, and the mixed $[1 \ 1 \ 1]^T$ polarization for the transmitter but a single electric-field component used in the inversion. The dimensions of the matrix \mathbf{A} in these three cases are $N_{tx}N_{ty}N_{rx}N_{ry} \times MPQ$, $3N_{tx}N_{ty}N_{rx}N_{ry} \times MPQ$, and $N_{tx}N_{ty}N_{rx}N_{ry} \times MPQ$, respectively, and the corresponding singular value variations are shown in Fig. 6(b)–(d), respectively. A direction observation is that the \hat{z} polarization of transceivers significantly deteriorates the reconstructable spectrum of the subsurface 3-D object. If both the transmitter and receiver are \hat{z} -polarized, i.e., the unit dipole source points at the \hat{z} -direction, and only E_z is used in FWI, the discrete operator \mathcal{I} has the least singular values, as shown by the “zz polarization” in Fig. 6(b). By contrast, if both the transmitter and receiver are horizontally polarized or one is horizontally polarized and another one is mixed polarized, the singular value variation curves almost overlap with those for the “no

polarization,” as shown in Fig. 6(b)–(d). However, if only the transmitter or only the receiver is \hat{z} -polarized, the singular value number of the matrix \mathbf{A} is intermediate. These phenomena are caused by the directivity pattern of an electric dipole. A \hat{z} -polarized electric dipole is unable to fully illuminate the subsurface 3-D objects. By reciprocity, a \hat{z} -polarized receiver is also unable to efficiently collect the EM signals scattered from the objects. As a result, the 3-D reconstructable spectrum of the subsurface object is narrowed down. In mathematics, this takes effects via the variation of \mathbf{f} in (10).

Since the right-singular functions can reflect the spatial distribution of the contrast based on (14), we apply the Fourier transforms to the first N right-singular vectors, and their summation actually represents the 3-D spectrum of the reconstructable contrast distribution when subsurface wave attenuation, evanescent mode contribution, and transceiver polarization are taken into account. Therefore, we define the spectrum

$$sp(\eta, \tau, \zeta) = \sum_{n=1}^N |\tilde{\mathbf{V}}_n(\eta, \tau, \zeta)| \quad (19)$$

where

$$\begin{aligned} \tilde{\mathbf{V}}_n(\eta, \tau, \zeta) &= \int_D \mathbf{V}_n(x, y, z) \exp[-j(\eta x + \tau y + \zeta z)] dx dy dz \\ &= \sum_{m,p,q} \mathbf{V}_n(x_m, y_p, z_q) \exp[-j(\eta x_m + \tau y_p + \zeta z_q)] \Delta V \end{aligned} \quad (20)$$

in which ΔV is the volume of each discrete voxel in the subsurface inversion domain and the ranges of η , τ , and ζ are set as $-30 \leq \eta \leq 30$, $-30 \leq \tau \leq 30$, and $0 \leq \zeta \leq 30$, respectively. Note that these ranges for η , τ , and ζ are large enough to incorporate all the spectral contents obtained from both theoretical analysis and SVD analysis according to (7a) and (11) as well as the background dielectric parameters and operation frequency. In addition, in order to guarantee the stability of the computed spectrum, N in (19) is set according to -20-dB SNR, i.e., the minimum singular value used in the computation is greater than 10% of the largest singular value Σ_1 . Numerical simulations show that the threshold of -20 dB is a practical value. The reconstructable spectra cannot be well represented if the threshold is too large. By contrast, further reducing the threshold value is not beneficial to refine the spectra but may deteriorate them due to the instability caused by numerical errors.

Fig. 7 shows the normalized 2-D slices of the computed spectra of right-singular functions for the five representative transceiver aperture sizes in Fig. 6(a) but with the polarization neglected. The corresponding 2-D slice of the theoretically reconstructable 3-D spectrum is also overlapped in each subfigure. We can see that the spectrum distribution of the right-singular functions is roughly consistent with the theoretically reconstructable spectrum of the subsurface scatterer. The right-singular function spectra also have the obvious “low-pass” feature in the horizontal xy plane and the “bandpass” feature in the vertical \hat{z} -direction when the transceiver aperture sizes in two horizontal directions are not large, as shown in

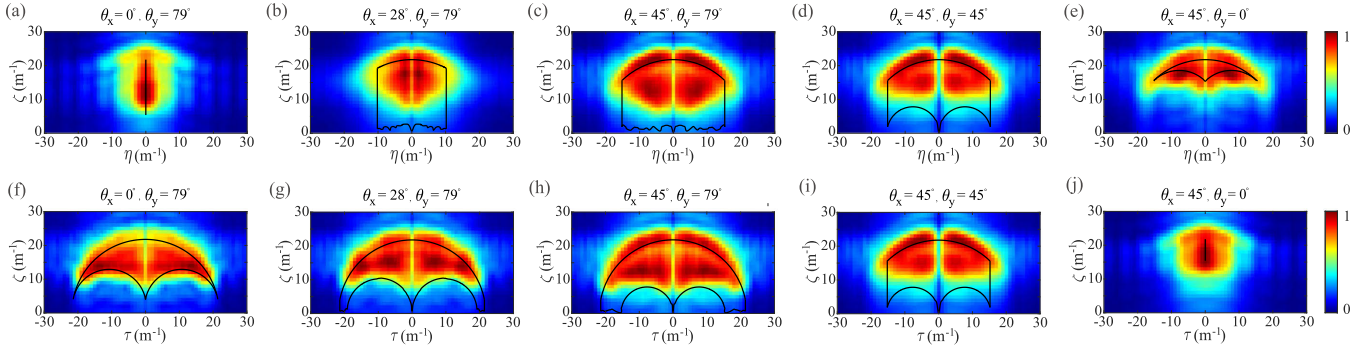


Fig. 7. Comparisons of the normalized 2-D slices of the spectra of right-singular functions obtained by SVD and 2-D slices of the 3-D theoretically reconstructable contrast spectra for five representative aperture sizes. The first row shows the $\eta\zeta$ slices at $\tau = 0$. The second row shows the $\tau\zeta$ slices at $\eta = 0$. Each theoretical 2-D spectrum is enclosed with a closed black curve.

Fig. 7(d), (e), (i), and (j). By contrast, as shown in Fig. 7(a)–(c), when the array aperture size in the \hat{y} -direction increases to $\theta_y = 79^\circ$, the right-singular function spectra in the $\eta\zeta$ plane have the obvious “allpass” feature in the vertical \hat{z} -direction. Other observations that can manifest the mutual coupling of two orthogonal directions include the remaining $\hat{\eta}$ -direction bandwidth when $\theta_x = 0^\circ$, as shown in Fig. 7(a), the broader 2-D $\tau\zeta$ spectrum bandwidth shown in Fig. 7(h) than that shown in Fig. 7(f) even both cases have the same \hat{y} -direction array aperture size, and the vertical “bandpass” feature in the $\eta\zeta$ plane shown in Fig. 7(c)–(e), although they have the same \hat{x} -direction transceiver aperture size. For 3-D MWI of subsurface objects, the wave propagates and is reflected or scattered in a 3-D space instead of being constrained inside a 2-D plane. As a result, the energy of the EM wave in two orthogonal directions is coupled instead of being independent. The last interesting observation is that the spectra of right-singular functions usually have more high-frequency contents than the theoretically reconstructable spectra. Such a phenomenon is also observed in [26, Fig. 4]. This is mainly due to the fact that the contribution from the evanescent wave is included when the spectra of right-singular functions are evaluated. The wavenumber of an evanescent EM wave is larger than the background k_b , which is manifested by the spectral contents located outside the theoretical high-frequency arc boundary in Fig. 7. In addition, it is assumed that the major energy of the incident and scattered waves concentrates in the plane waves when we compute the theoretically reconstructable spectra. However, when the spectra of right-singular functions are evaluated, the plane wave assumption for the incident and scattered waves is removed. Therefore, the subsurface scatterer is illuminated by EM waves at wider angles. The obtained reconstructable spectra are naturally broadened.

Fig. 8 shows the normalized 2-D slices of the magnitudes of the coefficients \mathbf{f} and the spectra of right-singular functions for five typical transceiver polarizations when the array aperture size is $\{\theta_x = 45^\circ, \theta_y = 79^\circ\}$. We can see that the difference between the spectra of right-singular functions with the transceiver polarization taken into account shown in Fig. 8(f)–(j) and (p)–(t) and the spectra shown in Fig. 7(c) and (h) for the configuration of “no polarization” is roughly consistent with the singular-value comparisons

between Fig. 6(a) and (b)–(d). When both the transmitter and receiver are horizontally polarized, although the bandwidths of the spectra shown in Fig. 8(f) and (p) are narrower than those shown in Fig. 7(c) and (h), the changes are marginal. However, the changes become obvious when only the transmitter is \hat{z} -polarized or only E_z is used in the reconstruction, as shown in Fig. 8(g), (i), (j), (q), (s), and (t). Also, they become significant when the transmitter is \hat{z} -polarized, and E_z simultaneously is used in the inversion, as shown in Fig. 8(h) and (r). The changes are mainly manifested by the loss of low-frequency contents of the 3-D reconstructable spectrum in the vertical \hat{z} -direction. Another interesting observation is the effects of the transceiver polarization on the magnitudes of the coefficients \mathbf{f} , as shown in Fig. 8(a)–(e) and (k)–(o). Obviously, the \hat{z} polarization leads to the more concentrated energy of the coefficient \mathbf{f} in the vertical direction, which weights the 3-D reconstructable spectra shown in Fig. 7(c) and (h) according to (10) and, thus, finally results in the loss of low-frequency contents shown in Fig. 8(g)–(j) and (q)–(t).

V. INFLUENCE OF THE 2-D TRANSCEIVER ARRAY APERTURE SIZE AND POLARIZATION ON 3-D SUBSURFACE FWI WITH BA: NUMERICAL VALIDATION

In this section, we validate the theoretical analysis results and the SVD analysis results presented in Sections III and IV via several numerical tests. The basic configurations of the inversion are the same as those mentioned in Section III. However, four cuboid scatterers are placed inside the inversion domain. They have the same dielectric parameters $\varepsilon_s = 3.2$ and $\sigma_s = 1.2$ mS/m. The centers of four scatterers are located at $(0.27, 0.27, 0.85)$ m, $(-0.27, 0.27, 0.85)$ m, $(0.27, -0.27, 0.85)$ m, and $(-0.27, -0.27, 0.85)$ m, respectively. Their dimensions are $0.36 \times 0.36 \times 0.36$ m, $0.12 \times 0.12 \times 0.36$ m, $0.12 \times 0.12 \times 0.36$ m, and $0.36 \times 0.36 \times 0.36$ m, respectively. The scattered electric fields recorded at the receiver array are synthesized by the stabilized biconjugate gradient fast Fourier transform (BCGS-FFT) solver [37]. The FWI is accomplished by the conjugate gradient solver based on the sensitivity matrix directly assembled by incident fields, i.e., based on BA. Also, the Tikhonov regularization factor for the least-square cost function is 0.001.

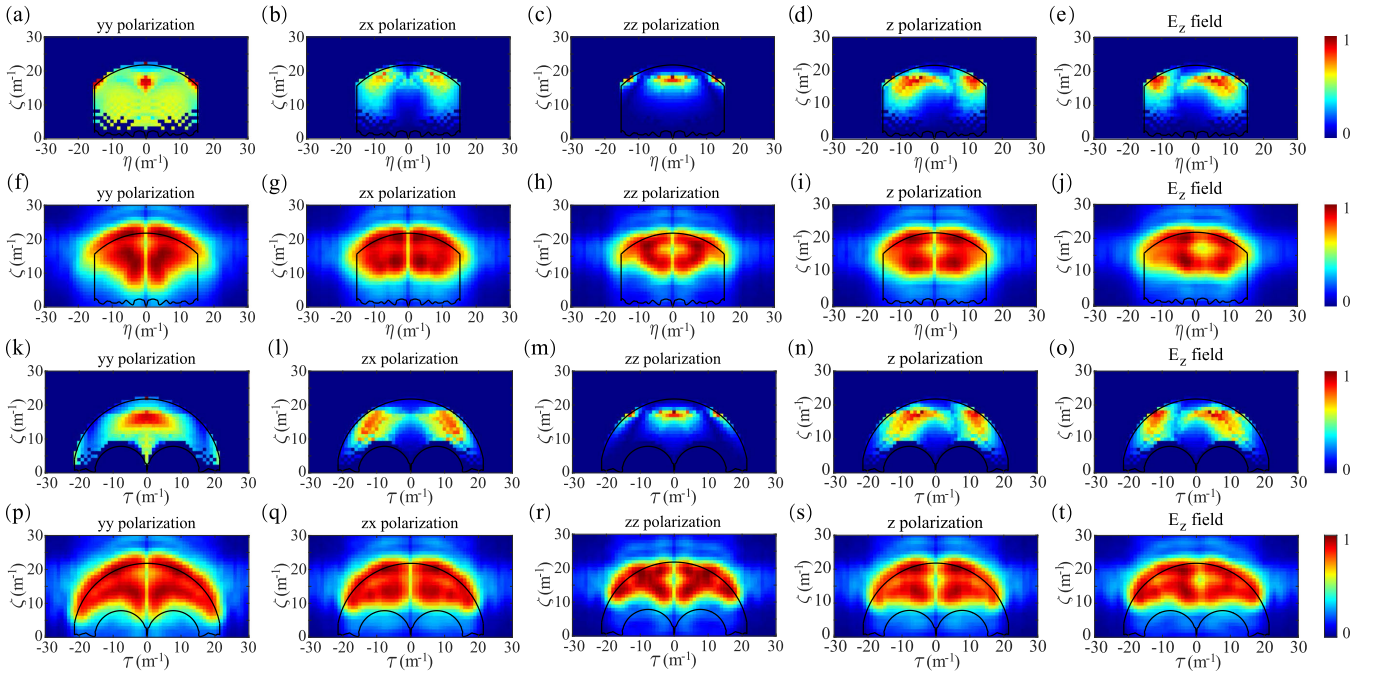


Fig. 8. Normalized 2-D slices of the magnitudes of the coefficients \mathbf{f} and the spectra of right-singular functions for different transceiver polarizations. The first row and the third row, respectively, show the $\eta\zeta$ slices at $\tau = 0$ and the $\tau\zeta$ slices at $\eta = 0$ of \mathbf{f} magnitudes. The second row and the fourth row, respectively, show the $\eta\zeta$ slices at $\tau = 0$ and the $\tau\zeta$ slices at $\eta = 0$ of the spectra of right-singular functions. From the 1st column to the 5th column, the transceiver has the polarization of "yy," "xz," and "zz," transmitter \hat{z} -polarized but all electric-field components used in inversion, and transmitter mixed $[1 \ 1 \ 1]^T$ polarized and only E_z used in inversion, respectively. Each theoretical 2-D spectrum is enclosed with a closed black curve.

Because certain polarizations of the transceivers must be taken into account in FWI, we choose the "yy polarization" to replace the no-polarization to validate the influence of the transceiver array size on the linear inversion results. Fig. 9 shows the reconstructed 3-D profiles of the contrast moduli of four scatterers as well as the 2-D slices at different positions for the aforementioned five typical 2-D transceiver aperture sizes when the excitation electric dipoles point at the \hat{y} -direction and E_y is used in the inversion. The model misfits of the five reconstructed 3-D contrast moduli profiles shown in Fig. 9(a)–(e) are 88.9%, 84.3%, 75.3%, 92.2%, and 97.4%, respectively, according to the definition given [38, eq. (16)]. Because we only consider the reconstructed scatterer shapes, which represent the spectral bandwidth, the large model misfit values caused by BA have no harm to the following analysis. Three observations are made. First, the "lowpass" phenomenon is obvious in the horizontal xy plane. As shown in the second row of Fig. 9, the highest horizontal resolution is achieved when the transceiver array has the largest 2-D aperture size with $\theta_x = 45^\circ$ and $\theta_y = 79^\circ$. In this situation, not only four scatterers are obviously separated, but also the boundary of each scatterer with respect to the background is clearly discerned. Compared with two big square scatterers, two small square scatterers have more blurry reconstructed boundaries. The reconstructed shapes almost become two circular disks. This difference is as we expect. Spectra of smaller scatterers have richer spatial high-frequency contents, and thus, their reconstructed profiles will be distorted more severely if the FWI operation is bandlimited. If we decrease the aperture size in the \hat{x} -direction to $\theta_x = 28^\circ$, the reconstruction resolution in the \hat{x} -direction severely deteriorates, and two scatterers cannot

be separated anymore, as shown in Fig. 9(g). However, two scatterers in the \hat{y} -direction are still separable. Also, this still holds even when we decrease θ_x to zero, as shown in Fig. 9(f). Second, the mutual coupling of the reconstructed profiles in the \hat{x} -direction and the \hat{y} -direction is obvious. By comparing the 2-D xy slices shown in Fig. 9(f)–(h), we can see that the resolution of the reconstruction in the \hat{y} -direction gradually deteriorates even when we keep the θ_y unchanged but gradually decrease the aperture size in the \hat{x} -direction. In addition, as shown in Fig. 9(f), four reconstructed scatterers still can be separated in the \hat{x} -direction although $\theta_x = 0^\circ$, which is caused by the large array aperture size in the \hat{y} -direction. Moreover, the reconstructed 2-D profile of the smaller scatterer shown in Fig. 9(p) deforms from the true shape more severely compared with that shown in Fig. 9(r), although the θ_y value is the same in both situations. The small transceiver array aperture size in the \hat{x} -direction also reduces the 2-D reconstructable spectrum bandwidth in the yz plane. Third, as shown by the comparisons between Fig. 9(l) and (m), although the θ_x has distinct values, the vertical resolution of the reconstructed 2-D profile in the xz plane almost keeps unchanged. This phenomenon actually indicates the vertical "allpass" feature inside the xz plane when the array aperture size in the orthogonal \hat{y} -direction is large enough, as illustrated in Fig. 7(b) and (c). However, if we decrease θ_y to 45° , as shown in Fig. 9(n), the vertical resolution of the reconstructed 2-D profile in the xz plane immediately deteriorates. In this situation, only the upper boundaries of the scatterers are discernible. The overall shapes of scatterers in the vertical direction almost become invisible, which indicates a loss of the spatial low-frequency contents of the reconstructed scatterer profiles. In other words, the vertical

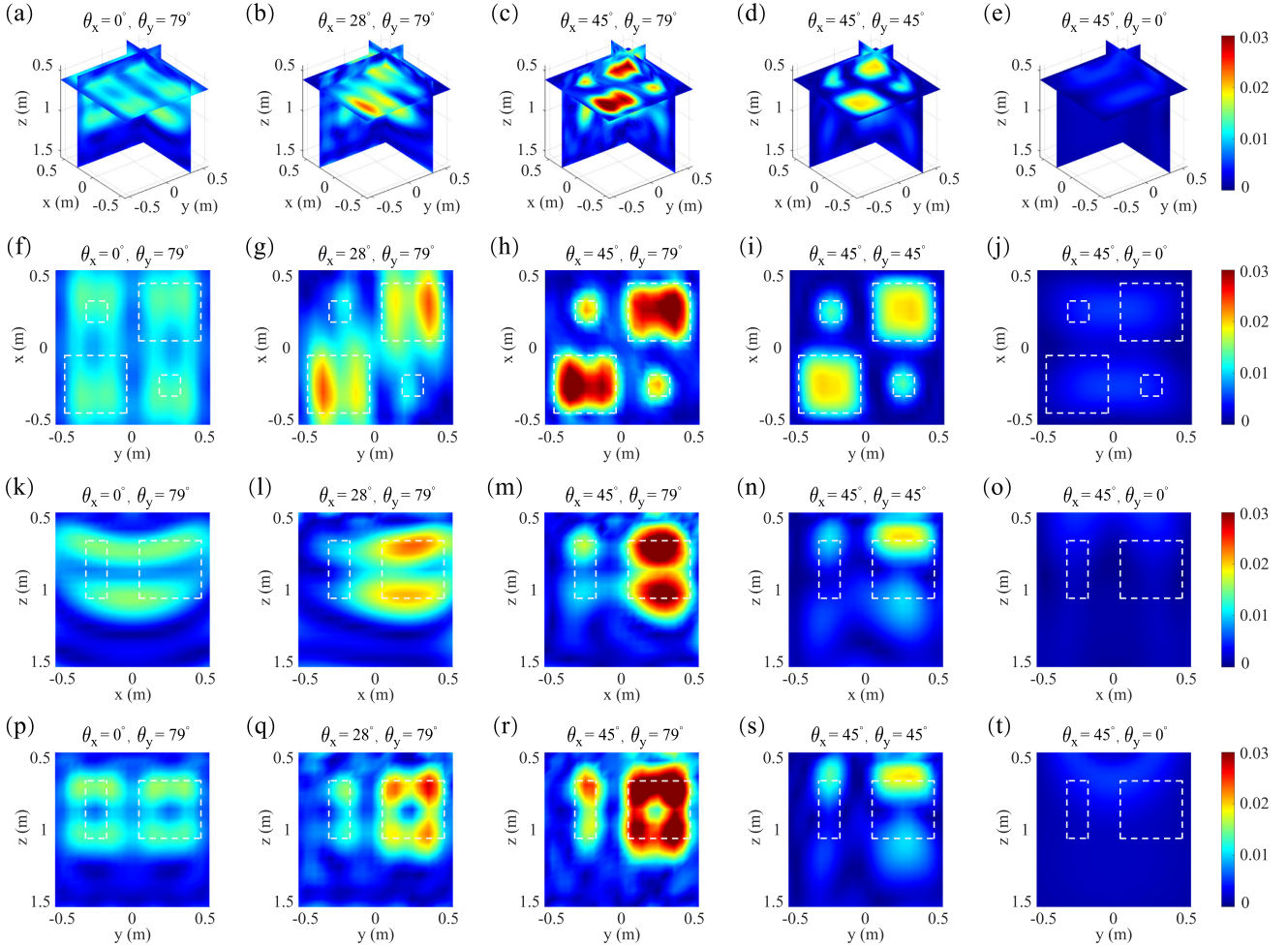


Fig. 9. Reconstructed contrast moduli distribution for the five representative transceiver aperture sizes. Different columns are corresponding to different aperture sizes. The first row shows the reconstructed 3-D profiles. The second, third, and fourth rows show the xy slices at $z = 0.61$ m, the xz slices at $y = 0.33$ m, and the yz slices at $x = 0.27$ m, respectively. White dotted boxes denote true shapes.

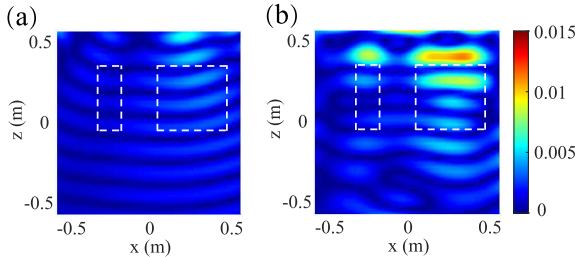


Fig. 10. Reconstructed 2-D xz profiles of the contrast moduli distribution for (a) $\theta_x = 28^\circ$ and (b) $\theta_x = 45^\circ$. White dotted boxes denote true shapes.

“bandpass” feature replaces the “allpass” feature. In order to further confirm this distinctive “allpass” feature in the 3-D reconstruction of subsurface objects, which is lacked in the 2-D problem, we also perform the BA-based 2-D FWI of two rectangular scatterers whose shapes coincide with the xz slices of the 3-D scatterers and dielectric parameters are also the same as those of the 3-D ones. As can be seen, compared with the 2-D slices shown in Fig. 9(l) and (m), the true reconstructed 2-D profiles shown in Fig. 10 for $\theta_x = 28^\circ$ and $\theta_x = 45^\circ$ only have the obvious upper boundaries of the scatterers. Especially, when $\theta_x = 28^\circ$, only the upper boundary of the big square scatterer can be located, and the overall

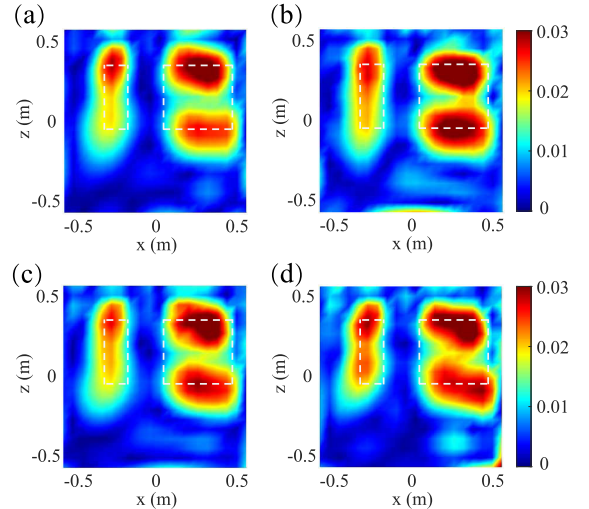


Fig. 11. xz slices of the reconstructed contrast moduli distribution for different transceiver polarizations when the array aperture has the size of $\theta_x = 45^\circ$ and $\theta_y = 79^\circ$. (a) zx polarization. (b) zz polarization. (c) Transmitter is \hat{z} -polarized, but all electric-field components are used in inversion. (d) Transmitter is mixed $[1 \ 1 \ 1]^T$ polarized, and only E_z is used in inversion. White dotted boxes denote true shapes.

shapes of both 2-D scatterers are completely lost, which is consistent with the “bandpass” feature shown in [26, Fig. 2].

Fig. 11 shows the xz slices of the reconstructed contrast moduli distribution for different transceiver polarizations when the 2-D array aperture has the size of $\theta_x = 45^\circ$ and $\theta_y = 79^\circ$. Compared with the xz slice shown in Fig. 9(m) for the “yy polarization,” we can see that the z polarization of the transmitter or the receiver almost has no harm to the reconstructed upper and lower boundaries of the big cuboid scatterer. However, the slowly varying \hat{z} -direction intermediate part of the big cuboid scatterer almost disappears in the reconstructed profiles shown in Fig. 11 but still can be seen in Fig. 9(m). This indicates that the transceiver z polarization actually filters out the vertical low-frequency contents of the scatterers in the reconstruction due to the electric dipole directivity pattern. This phenomenon is also observed in the reconstructable spectra obtained by SVD shown in Fig. 8.

VI. CONCLUSION AND FUTURE WORK

In this work, we have not only analyzed how the 2-D transceiver array aperture size and polarization influence the BA-based qualitative imaging of subsurface 3-D objects theoretically and based on SVD, but also implemented several numerical experiments to validate the analysis results. Compared with the influence of the 1-D array on 2-D reconstruction results given in previous works, that of the 2-D array on 3-D reconstruction results has similarities but also differences. The most significant similarity is that both the reconstructable spectra of subsurface 2-D and 3-D objects show the “lowpass” feature in the horizontal direction. In addition, phenomena such as more singular values of the integral operators observed for larger transceiver array aperture sizes and the high-frequency boundaries of the reconstructable spectra computed from the right-singular functions exceeding those from theoretical analysis, which have been observed in the 2-D problem, also show up in the 3-D reconstruction. The most significant difference is that the reconstructable 3-D spectrum has the obvious mutual coupling between horizontal directions, which are mainly manifested in two aspects: a transceiver array aperture size in one horizontal direction broadening the 2-D spectrum bandwidth in its orthogonal plane and the appearance of the vertical “allpass” feature in a vertical 2-D plane if the array aperture size in its orthogonal direction is large enough. Adding a dimension means wider incident and scattered angles of the EM wave in the horizontal plane, which, of course, leads to the inevitable coupling of the reconstructable 3-D spectrum in two horizontal directions. Meanwhile, adding a dimension leads to the transceiver polarization influence on the reconstructable spectra of subsurface objects, which has not been addressed in previous works. The SVD analysis and numerical experiments in this work have predicted and validated the polarization influence.

The future work will be focused on two aspects. The first one is to explore the influence of other factors in the transceiver array configuration, e.g., spatial sampling density of the scattered fields, antenna radiation pattern, noise level in measurement, multifrequency data, or even the vertical aperture size on the reconstructable spectra of 3-D subsurface objects. Their significant impacts in 2-D inversion have been studied in previous works [26], [27], [28], [29], [30], [31],

[39]. The second one is to investigate how the background layer configuration influences the 3-D reconstructable spectra. That is to say, we will study the reconstructability of 3-D objects embedded in a planarly multilayered medium.

APPENDIX A

We only discuss how to compute the spectral-domain layered DGF when the whole space is divided into two parts by the horizontal interface located at $z = z_1$. The medium located at $z < z_1$ has the dielectric parameters $\epsilon_1 \epsilon_0$ and μ_0 , while that located at $z > z_1$ has the dielectric parameters $\epsilon_2 \epsilon_0$ and μ_0 . The transmitter is located at (x_s, y_s, z_s) with $z_s < z_1$, and an arbitrary field point is located at (x, y, z) with $z > z_1$. The EM wave propagates from medium 1 to medium 2. Note that we have $z_1 = 0$ and $\epsilon_1 = 1$ in our problem. According to the transmission-line analogy method presented in [34], the spectral domain $\tilde{\mathbf{G}}(\mathbf{k}'_\rho, z, z_s)$ in (5b) can be evaluated by

$$\tilde{\mathbf{G}}(\mathbf{k}'_\rho, z, z_s) = \begin{bmatrix} \tilde{g}_{xx}(z|z_s) & \tilde{g}_{xy}(z|z_s) & \tilde{g}_{xz}(z|z_s) \\ \tilde{g}_{yx}(z|z_s) & \tilde{g}_{yy}(z|z_s) & \tilde{g}_{yz}(z|z_s) \\ \tilde{g}_{zx}(z|z_s) & \tilde{g}_{zy}(z|z_s) & \tilde{g}_{zz}(z|z_s) \end{bmatrix} \quad (A1)$$

where

$$\tilde{g}_{xx}(z|z_s) = -\frac{k_x'^2}{k_\rho'^2} V_i^e(z|z_s) - \frac{k_y'^2}{k_\rho'^2} V_i^h(z|z_s) \quad (A2a)$$

$$\tilde{g}_{xy}(z|z_s) = -\frac{k_x' k_y'}{k_\rho'^2} V_i^e(z|z_s) + \frac{k_x' k_y'}{k_\rho'^2} V_i^h(z|z_s) \quad (A2b)$$

$$\tilde{g}_{xz}(z|z_s) = \frac{k_x'}{\omega \epsilon_1 \epsilon_0} V_v^e(z|z_s) \quad (A2c)$$

$$\tilde{g}_{yx}(z|z_s) = -\frac{k_x' k_y'}{k_\rho'^2} V_i^e(z|z_s) + \frac{k_x' k_y'}{k_\rho'^2} V_i^h(z|z_s) \quad (A2d)$$

$$\tilde{g}_{yy}(z|z_s) = -\frac{k_y'^2}{k_\rho'^2} V_i^e(z|z_s) - \frac{k_x'^2}{k_\rho'^2} V_i^h(z|z_s) \quad (A2e)$$

$$\tilde{g}_{yz}(z|z_s) = \frac{k_y'}{\omega \epsilon_1 \epsilon_0} V_v^e(z|z_s) \quad (A2f)$$

$$\tilde{g}_{zx}(z|z_s) = \frac{k_x'}{\omega \epsilon_2 \epsilon_0} I_i^e(z|z_s) \quad (A2g)$$

$$\tilde{g}_{zy}(z|z_s) = \frac{k_y'}{\omega \epsilon_2 \epsilon_0} I_i^e(z|z_s) \quad (A2h)$$

$$\tilde{g}_{zz}(z|z_s) = -\frac{k_\rho'^2}{\omega^2 \epsilon_1 \epsilon_2 \epsilon_0^2} I_v^e(z|z_s) \quad (A2i)$$

where the superscript e stands for the transverse magnetic (TM) mode, while the superscript h stands for the transverse electric (TE) mode. The voltage and current terms are evaluated by

$$V_i^p(z|z_s) = \frac{Z_1^p}{2} (1 + \Gamma_{21}^p) \exp[-jk'_z(z_1 - z_s)] \\ \cdot \exp[-jk'_z(z - z_1)] \quad (A3a)$$

$$V_v^p(z|z_s) = \frac{1}{2} (1 + \Gamma_{21}^p) \exp[-jk'_z(z_1 - z_s)] \\ \cdot \exp[-jk'_z(z - z_1)] \quad (A3b)$$

$$\begin{aligned} I_i^p(z|z_s) &= \frac{1}{2}(1 - \Gamma_{21}^p) \exp[-jk'_{z1}(z_1 - z_s)] \\ &\quad \cdot \exp[-jk'_{z2}(z - z_1)] \end{aligned} \quad (\text{A3c})$$

$$\begin{aligned} I_v^p(z|z_s) &= \frac{1}{2Z_1^p}(1 - \Gamma_{21}^p) \exp[-jk'_{z1}(z_1 - z_s)] \\ &\quad \cdot \exp[-jk'_{z2}(z - z_1)] \end{aligned} \quad (\text{A3d})$$

where the superscript p can be e or h and

$$\Gamma_{21}^p = \frac{Z_2^p - Z_1^p}{Z_2^p + Z_1^p} \quad (\text{A4})$$

is the reflection coefficient when the EM wave propagates from medium 1 to medium 2. $Z_n^e = (k'_{zn}/\omega\epsilon_n\epsilon_0)$ and $Z_n^h = (\omega\mu_n\mu_0/k'_{zn})$ are the characteristic impedances in the n th layer for the TM mode and the TE mode, respectively. In addition, the superscript apostrophe means the EM wave is emitted from the source point at (x_s, y_s, z_s) .

$\tilde{\mathbf{G}}(\mathbf{k}_\rho, z_r, z)$ in (5a) can be derived following the similar procedure. The only difference is that the EM wave propagates from the field point (x, y, z) located inside medium 2 to the receiver point (x_r, y_r, z_r) located inside medium 1. Therefore, we must replace $z|z_s$ with $z_r|z$ in (A1) and (A2), replace ϵ_1 with ϵ_2 and replace ϵ_2 with ϵ_1 in (A2), drop the superscript apostrophe in (A2), replace Z_1^p with Z_2^p and replace Γ_{21}^p with Γ_{12}^p in (A3), replace $[-jk'_{z1}(z_1 - z_s)]$ with $[jk'_{z2}(z_1 - z)]$ in (A3), replace $[-jk'_{z2}(z - z_1)]$ with $[jk'_{z1}(z_r - z_1)]$ in (A3), and exchange Z_1^p and Z_2^p in (A4) to compute Γ_{12}^p .

APPENDIX B

We define

$$\tilde{\mathbf{I}} = \tilde{\mathbf{G}}(\mathbf{k}_\rho, z_r, z)\tilde{\mathbf{G}}(\mathbf{k}'_\rho, z, z_s) \cdot \mathbf{J}(\mathbf{r}_s) \quad (\text{B1})$$

where $\tilde{\mathbf{I}}$ is a column vector having three elements corresponding to the \hat{x} , \hat{y} , and \hat{z} components of the scattered electric fields. In addition, $\tilde{\mathbf{I}}$ is not only determined by the specific expression of $\tilde{\mathbf{G}}$ given in Appendix A, but also changes with the polarization of the excitation source \mathbf{J} . Therefore, we use double subscripts to denote the component of $\tilde{\mathbf{I}}$. For example, \tilde{I}_{xy} stands for the 1st \hat{x} component of $\tilde{\mathbf{I}}$ but is excited by a unit electric dipole having the \hat{y} polarization. In the following, we take \tilde{I}_{xy} as an example to show how to derive $\tilde{\mathbf{I}}$. By substituting the expressions given in Appendix A into $\tilde{\mathbf{G}}$ and letting \mathbf{J} be equal to $[0 \ 1 \ 0]^T$, we obtain

$$\begin{aligned} \tilde{I}_{xy} &= \tilde{g}_{xx}(z_r|z)\tilde{g}_{xy}(z|z_s) + \tilde{g}_{xy}(z_r|z)\tilde{g}_{yy}(z|z_s) \\ &\quad + \tilde{g}_{xz}(z_r|z)\tilde{g}_{zy}(z|z_s) \\ &= \left[-\frac{k_x^2}{k_\rho^2} \frac{k_{z1}k_{z2}}{\omega\epsilon_2\epsilon_0k_{z1} + \omega\epsilon_1\epsilon_0k_{z2}} - \frac{k_y^2}{k_\rho^2} \frac{\omega\mu_0}{k_{z1} + k_{z2}} \right] \\ &\quad \times \left[-\frac{k'_xk'_y}{k_\rho^2} \frac{k'_{z1}k'_{z2}}{\omega\epsilon_1\epsilon_0k'_{z2} + \omega\epsilon_2\epsilon_0k'_{z1}} + \frac{k'_xk'_y}{k_\rho^2} \frac{\omega\mu_0}{k'_{z1} + k'_{z2}} \right] \\ &\quad + \left[-\frac{k_xk_y}{k_\rho^2} \frac{k_{z1}k_{z2}}{\omega\epsilon_2\epsilon_0k_{z1} + \omega\epsilon_1\epsilon_0k_{z2}} + \frac{k_xk_y}{k_\rho^2} \frac{\omega\mu_0}{k_{z1} + k_{z2}} \right] \\ &\quad \times \left[-\frac{k_y^2}{k_\rho^2} \frac{k'_{z1}k'_{z2}}{\omega\epsilon_1\epsilon_0k'_{z2} + \omega\epsilon_2\epsilon_0k'_{z1}} - \frac{k_x^2}{k_\rho^2} \frac{\omega\mu_0}{k'_{z1} + k'_{z2}} \right] \end{aligned}$$

$$\begin{aligned} &- \frac{k_xk'_y}{\omega^2} \frac{k_{z1}}{k_{z1}\epsilon_2\epsilon_0 + k_{z2}\epsilon_1\epsilon_0} \frac{k'_{z1}}{k'_{z2}\epsilon_1\epsilon_0 + k'_{z1}\epsilon_2\epsilon_0} \Big\} \\ &\quad \cdot \exp[jk_{z1}z_r + jk'_{z1}z_s] \exp[-j(k_{z2} + k'_{z2})z] \\ &= f_{xy} \cdot \exp[-j(k_{z2} + k'_{z2})z] \end{aligned} \quad (\text{B2})$$

where f_{xy} is the \hat{x} component of the vector \mathbf{f} defined in (8) when the excitation electric dipole is \hat{y} -polarized. Following the similar procedure, we can also derive other eight components \tilde{I}_{xx} , \tilde{I}_{xz} , \tilde{I}_{yx} , \tilde{I}_{yy} , \tilde{I}_{yz} , \tilde{I}_{zx} , \tilde{I}_{zy} , and \tilde{I}_{zz} . The difference among these components completely depends on the specific expression of the coefficient f , which is actually determined by the polarization of the excitation electric source and which scattered electric-field component is used in the reconstruction. In other words, by referring to (10), we can claim that the inversion performance will be exactly the same if we neglect the source polarization and the field component used in the inversion.

REFERENCES

- [1] M. Pastorino, *Microwave Imaging*. Singapore: Wiley, 2010.
- [2] Z. Luo et al., “Quantitative reconstruction of dielectric properties based on deep-learning-enabled microwave-induced thermoacoustic tomography,” *IEEE Trans. Microw. Theory Techn.*, vol. 71, no. 6, p. 2652, Jun. 2023.
- [3] Y. Meng, C. Lin, J. Zang, A. Qing, and N. K. Nikolova, “General theory of holographic inversion with linear frequency modulation radar and its application to whole-body security scanning,” *IEEE Trans. Microw. Theory Techn.*, vol. 68, no. 11, pp. 4694–4705, Nov. 2020.
- [4] Y. Zhou et al., “Learning-based subsurface quantitative imaging via near-field scanning microwave microscopy,” *IEEE Trans. Microw. Theory Techn.*, vol. 70, no. 11, pp. 5008–5018, Nov. 2022.
- [5] J. D. Chisum and Z. Popovic, “Performance limitations and measurement analysis of a near-field microwave microscope for nondestructive and subsurface detection,” *IEEE Trans. Microw. Theory Techn.*, vol. 60, no. 8, pp. 2605–2615, Aug. 2012.
- [6] C. Li and K. Sun, “Rigorous formulation for retrieving electromagnetic parameters of biaxial composite material with rectangular waveguide,” *IEEE Trans. Microw. Theory Techn.*, early access, Feb. 26, 2024, doi: [10.1109/TMTT.2024.3371949](https://doi.org/10.1109/TMTT.2024.3371949).
- [7] L. Wang, Y. Zhang, F. Han, J. Zhou, and Q. H. Liu, “A phaseless inverse source method (PISM) based on near-field scanning for radiation diagnosis and prediction of PCBs,” *IEEE Trans. Microw. Theory Techn.*, vol. 68, no. 10, pp. 4151–4160, Oct. 2020.
- [8] L. Ding, X. L. Deán-Ben, and D. Razansky, “Real-time model-based inversion in cross-sectional optoacoustic tomography,” *IEEE Trans. Med. Imag.*, vol. 35, no. 8, pp. 1883–1891, Aug. 2016.
- [9] K. Ren, Q. Wang, and R. J. Burkholder, “A fast back-projection approach to diffraction tomography for near-field microwave imaging,” *IEEE Antennas Wireless Propag. Lett.*, vol. 18, pp. 2170–2174, 2019.
- [10] W. Zhang and A. Hoofar, “Three-dimensional real-time through-the-wall radar imaging with diffraction tomographic algorithm,” *IEEE Trans. Geosci. Remote Sens.*, vol. 51, no. 7, pp. 4155–4163, Jul. 2013.
- [11] I. Catapano, L. Crocco, and T. Isernia, “Improved sampling methods for shape reconstruction of 3-D buried targets,” *IEEE Trans. Geosci. Remote Sens.*, vol. 46, no. 10, pp. 3265–3273, Oct. 2008.
- [12] M. Zhong, Y. Chen, J. Li, and F. Han, “Reconstruction of subsurface objects by LSM and FWI from limited-aperture electromagnetic data,” *IEEE Trans. Geosci. Remote Sens.*, vol. 60, 2022, Art. no. 2003011.
- [13] H. Liu, Z. Long, F. Han, G. Fang, and Q. H. Liu, “Frequency-domain reverse-time migration of ground penetrating radar based on layered medium Green’s functions,” *IEEE J. Sel. Topics Appl. Earth Observ. Remote Sens.*, vol. 11, no. 8, pp. 2957–2965, Aug. 2018.
- [14] X. Zhuge, A. G. Yarovoy, T. Savelyev, and L. Lighthart, “Modified Kirchhoff migration for UWB MIMO array-based radar imaging,” *IEEE Trans. Geosci. Remote Sens.*, vol. 48, no. 6, pp. 2692–2703, Jun. 2010.
- [15] F. Li, Q. H. Liu, and L.-P. Song, “Three-dimensional reconstruction of objects buried in layered media using Born and distorted Born iterative methods,” *IEEE Geosci. Remote Sens. Lett.*, vol. 1, no. 2, pp. 107–111, Apr. 2004.

- [16] Y. Altuncu, T. Durukan, and R. E. Akdogan, "Reconstruction of two-dimensional objects buried into three-part space with locally rough interfaces via distorted Born iterative method," *Prog. Electromagn. Res.*, vol. 166, pp. 23–41, 2019.
- [17] J. Zhuo, L. Ye, F. Han, L. Xiong, and Q. H. Liu, "Multiparametric electromagnetic inversion of 3-D biaxial anisotropic objects embedded in layered uniaxial media using VBIM enhanced by structural consistency constraint," *IEEE Trans. Antennas Propag.*, vol. 68, no. 6, pp. 4774–4785, Jun. 2020.
- [18] E. Tetik and I. Akduman, "3D imaging of dielectric objects buried under a rough surface by using CSI," *Int. J. Antennas Propag.*, vol. 2015, pp. 1–7, 2015.
- [19] T. Lu, K. Agarwal, Y. Zhong, and X. Chen, "Through-wall imaging: Application of subspace-based optimization method," *Prog. Electromagn. Res.*, vol. 102, pp. 351–366, 2010.
- [20] X. Ye and X. Chen, "Subspace-based distorted-Born iterative method for solving inverse scattering problems," *IEEE Trans. Antennas Propag.*, vol. 65, no. 12, pp. 7224–7232, Dec. 2017.
- [21] N. Zaiping, Y. Feng, Z. Yanwen, and Z. Yerong, "Variational Born iteration method and its applications to hybrid inversion," *IEEE Trans. Geosci. Remote Sens.*, vol. 38, no. 4, pp. 1709–1715, Jul. 2000.
- [22] K. Agarwal, R. Song, M. D'Urso, and X. Chen, "Improving the performances of the contrast source extended Born inversion method by subspace techniques," *IEEE Geosci. Remote Sens. Lett.*, vol. 10, no. 2, pp. 391–395, Mar. 2013.
- [23] L. Di Donato, R. Palmeri, G. Sorbello, T. Isernia, and L. Crocco, "A new linear distorted-wave inversion method for microwave imaging via virtual experiments," *IEEE Trans. Microw. Theory Techn.*, vol. 64, no. 8, pp. 2478–2488, Aug. 2016.
- [24] M. T. Bevacqua and T. Isernia, "An effective rewriting of the inverse scattering equations via Green's function decomposition," *IEEE Trans. Antennas Propag.*, vol. 69, no. 8, pp. 4883–4893, Aug. 2021.
- [25] M. T. Bevacqua and T. Isernia, "Support reconstruction of dielectric and metallic targets via the contraction integral equation," *IEEE Trans. Antennas Propag.*, vol. 72, no. 3, pp. 2643–2653, Mar. 2024.
- [26] G. Leone and F. Soldovieri, "Analysis of the distorted Born approximation for subsurface reconstruction: Truncation and uncertainties effects," *IEEE Trans. Geosci. Remote Sens.*, vol. 41, no. 1, pp. 66–74, Jan. 2003.
- [27] R. Persico, R. Bernini, and F. Soldovieri, "The role of the measurement configuration in inverse scattering from buried objects under the Born approximation," *IEEE Trans. Antennas Propag.*, vol. 53, no. 6, pp. 1875–1887, Jun. 2005.
- [28] O. M. Bucci, L. Crocco, T. Isernia, and V. Pascazio, "Inverse scattering problems with multifrequency data: Reconstruction capabilities and solution strategies," *IEEE Trans. Geosci. Remote Sens.*, vol. 38, no. 4, pp. 1749–1756, Jul. 2000.
- [29] R. Persico, F. Soldovieri, and G. Leone, "A microwave tomographic imaging approach for multibistatic configuration: The choice of the frequency step," *IEEE Trans. Instrum. Meas.*, vol. 55, no. 6, pp. 1926–1934, Dec. 2006.
- [30] H. Liu et al., "Migration of ground penetrating radar with antenna radiation pattern correction," *IEEE Geosci. Remote Sens. Lett.*, vol. 19, 2022, Art. no. 3500805.
- [31] F. Soldovieri, R. Persico, and G. Leone, "Effect of source and receiver radiation characteristics in subsurface prospecting within the distorted Born approximation," *Radio Sci.*, vol. 40, no. 3, pp. 1–13, Jun. 2005.
- [32] G. Gennarelli and F. Soldovieri, "The effect of array configuration in transmission-mode electromagnetic imaging," *IEEE Trans. Antennas Propag.*, vol. 62, no. 10, pp. 5148–5156, Oct. 2014.
- [33] G. Gennarelli, I. Catapano, F. Soldovieri, and R. Persico, "On the achievable imaging performance in full 3-D linear inverse scattering," *IEEE Trans. Antennas Propag.*, vol. 63, no. 3, pp. 1150–1155, Mar. 2015.
- [34] K. A. Michalski and J. R. Mosig, "Multilayered media Green's functions in integral equation formulations," *IEEE Trans. Antennas Propag.*, vol. 45, no. 3, pp. 508–519, Mar. 1997.
- [35] M. Bertero and P. Boccacci, *Introduction to Inverse Problems in Imaging*. Boca Raton, FL, USA: CRC Press, 1998.
- [36] S. Twomey, *Introduction to the Mathematics of Inversion in Remote Sensing and Indirect Measurements*. New York, NY, USA: Dover, 1977.
- [37] F. Han, J. Zhuo, N. Liu, Y. Liu, H. Liu, and Q. H. Liu, "Fast solution of electromagnetic scattering for 3-D inhomogeneous anisotropic objects embedded in layered uniaxial media by the BCGS-FFT method," *IEEE Trans. Antennas Propag.*, vol. 67, no. 3, pp. 1748–1759, Mar. 2019.
- [38] T. Lan, N. Liu, F. Han, and Q. H. Liu, "Joint petrophysical and structural inversion of electromagnetic and seismic data based on volume integral equation method," *IEEE Trans. Geosci. Remote Sens.*, vol. 57, no. 4, pp. 2075–2086, Apr. 2019.
- [39] F. Soldovieri and R. Persico, "Reconstruction of an embedded slab from multifrequency scattered field data under the distorted Born approximation," *IEEE Trans. Antennas Propag.*, vol. 52, no. 9, pp. 2348–2356, Sep. 2004.



Kemeng Tao received the B.E. degree in electronic information engineering from Xiangtan University, Xiangtan, China, in 2020. She is currently pursuing the master's degree with Xiamen University, Xiamen, China.

Her research interests include electromagnetic inverse scattering and antenna array configuration for electromagnetic full-wave inversion.



Sijia Ma received the B.S. degree in electronic information science and technologies from Shaanxi Normal University, Xi'an, China, in 2021. She is currently pursuing the master's degree with Xiamen University, Xiamen, China.

Her research interests include electromagnetic inverse scattering and antenna array configuration for electromagnetic full-wave inversion.



Feng Han (Senior Member, IEEE) received the B.S. degree in electronic science from Beijing Normal University, Beijing, China, in 2003, the M.S. degree in geophysics from Peking University, Beijing, in 2006, and the Ph.D. degree in electrical engineering from Duke University, Durham, NC, USA, in 2011.

From 2011 to 2015, he was a Software Engineer at Wavenovation, Inc., Xiamen, China. In July 2015, he joined the Institute of Electromagnetics and Acoustics, Xiamen University, Xiamen, as an Assistant Professor and was promoted to Associate Professor there in 2020. In October 2023, he joined the School of Computing and Information Technology, Great Bay University, Dongguan, China, as an Associate Professor. He has published over 50 articles in refereed journals. His research interests include electromagnetic scattering and inverse scattering in complex media, multiparametric and multidimensional hybrid electromagnetic full-wave inversion, fast electromagnetic full-wave inversion based on scientific machine learning, configuration of the antenna array for electromagnetic inverse problems, and geophysical electromagnetic exploration and inversion.